# Use of polarimetric lidar for the study of oriented ice plates in clouds

Massimo Del Guasta, Edgar Vallar, Olivier Riviere, Francesco Castagnoli, Valerio Venturi, and Marco Morandi

A polarization lidar operating at 532 nm was converted into an automatic, polarimetric lidar capable of measuring the entire Stokes vector of backscattered light and its derived quantities. Among these quantities, circular and linear depolarizations were studied as tools for investigating the presence of anisotropic scattering media. Isotropic scatterers show a simple relationship between linear and circular depolarization, a relation that we confirm theoretically and experimentally. Deviations from this relation, which are possible in the presence of anisotropic scatterers such as horizontally oriented ice plates when they are observed with a slant lidar, were studied both numerically and experimentally. 

*OCIS codes:* 010.3640, 010.2940, 010.1310, 260.5430.

## 1. Introduction

Elastic backscatter lidar is perhaps the most widespread and robust kind of lidar. Polarization lidar measurements discriminate cloud phase and yield indications of ice particle shape and orientation[1] through variations in linear depolarization ratio $\delta_l$. This ratio can be defined as the ratio of the orthogonal to parallel polarized components of the backscattered laser power. Polarization lidars also provide experimental evidence of the anisotropic scattering behavior of horizontally oriented ice plates, which are often present in high clouds. The nondepolarized, specular reflection of these particles is easily detected by means of zenith-pointing[2] and scanning[3] lidars. Unfortunately, depolarization information is only a part of the polarization-related information contained in the backscattered signal. A complete characterization of the polarization state of backscattered light is, in fact, contained in the entire Stokes vector,[4] $S = (I, Q, U, V)^T$. The ordinary lidar linear depolarization, defined as the ratio

$$\delta_l = \frac{I_s}{I_p} = \frac{I - Q}{I + Q} \tag{1}$$

(in which $I_p$ and $I_s$ are, respectively, the backscatter intensities received with polarization parallel and perpendicular to the laser linear polarization), is simply a combination of the first two elements of $S$. $U$ and $V$ are lost in the process.

In the past, several researchers[5–7] used complex lidar systems to obtain a complete characterization of the Mueller matrices of ice particles. The additional information provided by these complex systems did not justify the effort required for the routine operation of these instruments, and these research projects were apparently abandoned. We have converted a simple polarization lidar into an automatic polarimetric lidar simply by adding a PC-controlled phase retarder along the laser beam and PC-controlled ferroelectric phase retarders just in front of the polarization analyzer of the receiving section. The upgraded system was found to be suitable for determining the Stokes vector of backscattered light in routine cloud measurements. The principal application of the instrument is in the detection of oriented ice plates of ideal hexagonal geometry in clouds by means of a simultaneous analysis of linear and circular depolarization: two quantities that can be derived from Stokes vectors. The lidar was tilted 30° off zenith to introduce an anisotropy into the backscattering in the presence of horizontally oriented

M. Del Guasta (m.delguasta@ifac.enr.it), F. Castagnoli, V. Venturi, and M. Morandi are with the Istituto Fisica Applicata "Nello Carrara" (IFAC), Consiglio Nazionale delle Ricerche, Florence, Italy. E. Vallar is with the Department of Physics, De La Salle University, Manila, Philippines. O. Riviere is with the Département de Physique, Ecole Normale Supérieure, Paris, France.

Received 28 June 2005; revised 13 December 2005; accepted 27 January 2006; posted 7 February 2006 (Doc. ID 63076).

0003-6935/06/204878-10$15.00/0

Table 1. Specifications of Our Lidar

| Measurand | Property or Value |
|---|---|
| Laser | Quantel Brilliant Nd:YAG, 400 mJ, 532 nm |
| Repetition rate | 20 Hz |
| Emitter $\lambda/4$ plate | Casix zeroth-order, air spaced |
| Telescope | Refractive, achromatic, f = 30 cm, diameter = 8 cm |
| Field of view | 0.6 mrad |
| Filter | Andover, 532 nm, 0.19 nm bandwidth |
| FE cells | Glued stack of three Displaytech LV1300-OEM-UV-QWPs |
| Polarizer cubes | Casix PBS0101-532 |
| Photomultipliers | Hamamatsu R4124 |
| Acquisition system | Licel GmbH, analog 12 bit, 7.5 m resolution |

ideal ice plates. On the basis of numerical simulations, this anisotropy is expected to produce an anomalous relation between linear and circular depolarization. Simulations were also carried out on deformed plates for an understanding of the usefulness of the method in detecting oriented plates in real-world clouds. The first experimental results obtained in midlatitude cirrus and ice-precipitating altocumulus clouds are discussed.

## 2. Methods

A small, automatic polarization lidar, developed at the Institute of Applied Physics, Consiglio Nazionale delle Ricerche, and based on a Nd:YAG laser (Table 1), was equipped with a zeroth-order $\lambda/4$ plate along the output laser beam. The plate could be bistatically rotated by 0° and 45° by a PC-driven rotating electromagnet. In this way, pure linear or circular polarization can be sent into the atmosphere. To obtain a complete analysis of the received polarized light, we inserted an optical element consisting of a stack of three ferroelectric (FE) $\lambda/4$ phase rotators just in front of the polarization analyzer. To reduce the cross talk between the two polarization channels, the polarization analyzer was made from three polarizing cube beam splitters, as in Fig. 1. The polarimetric lidar has no scanning features but can easily be tilted off-zenith as a whole.

If $\mathbf{S}_0 = (I_0, Q_0, U_0, V_0)^T$ is the Stokes vector of the laser light sent into the atmosphere and $\mathbf{S} = (I, Q, U, V)^T$ is the Stokes vector of the backscattered light, voltage signals $v_1$ and $v_2$ at the two photomultiplier tubes (PMTs) are given by

$$v_1 = G_1 \frac{K}{R^2} [1 \quad 0 \quad 0 \quad 0]^* \mathbf{M}_{\mathrm{POL}_1}{}^* \mathbf{M}_{\mathrm{FE}}{}^* \mathbf{M}_{\mathrm{DM}}{}^* \mathbf{M}_{\mathrm{ATM}}{}^* \mathbf{S}_0,$$

$$v_2 = G_2 \frac{K}{R^2} [1 \quad 0 \quad 0 \quad 0]^* \mathbf{M}_{\mathrm{POL}_2}{}^* \mathbf{M}_{\mathrm{FE}}{}^* \mathbf{M}_{\mathrm{DM}}{}^* \mathbf{M}_{\mathrm{ATM}}{}^* \mathbf{S}_0,$$

where $G_1$ and $G_2$ are the PMT sensitivities, $K$ is a scalar instrumental constant, $R$ is the lidar range, and $\mathbf{M}_{\mathrm{POL}_1}$, $\mathbf{M}_{\mathrm{POL}_2}$, $\mathbf{M}_{\mathrm{FE}}$, and $\mathbf{M}_{\mathrm{DM}}$ are the $4 \times 4$ Mueller matrices of, respectively, the two channels of the polarization analyzer, the FE cell stack, and the receiver's dichroic mirror. $\mathbf{M}_{\mathrm{ATM}}$ is the 180° backscatter Mueller matrix per unit of volume of atmosphere. The Mueller matrix of the sending mirror was disregarded because it operates on linearly polarized light directed along the $s$ axis of the mirror. The Mueller matrix of the emitter $\lambda/4$ plate was also disregarded (see Appendix A). In what follows, matrices for the ideal optical components are used for the sake of simplicity.

The polarization analyzer is aligned such that PMT 2 and PMT 1 receive, respectively, light that is polarized parallel and perpendicular to the laser linear polarization adopted (Fig. 1), so the Mueller matrices of the ideal polarization analyzer for the two receiving channels are

$$\mathbf{M}_{\mathrm{POL}_1} = \begin{bmatrix} 1 & -1 & 0 & 0 \\ -1 & 1 & 0 & 0 \\ 0 & 0 & 0 & 0 \\ 0 & 0 & 0 & 0 \end{bmatrix}, \quad \mathbf{M}_{\mathrm{POL}_2} = \begin{bmatrix} 1 & 1 & 0 & 0 \\ 1 & 1 & 0 & 0 \\ 0 & 0 & 0 & 0 \\ 0 & 0 & 0 & 0 \end{bmatrix}. \tag{3}$$

PMT 1 channel PMT 2 channel

Each of the three FE cells acted as a $\lambda/4$ plate, the axis of which could be aligned with or rotated 45° with respect to the cube analyzer by means of a transistor–transistor logic signal provided by the PC (Fig. 1). Each FE cell has two Mueller matrices, one

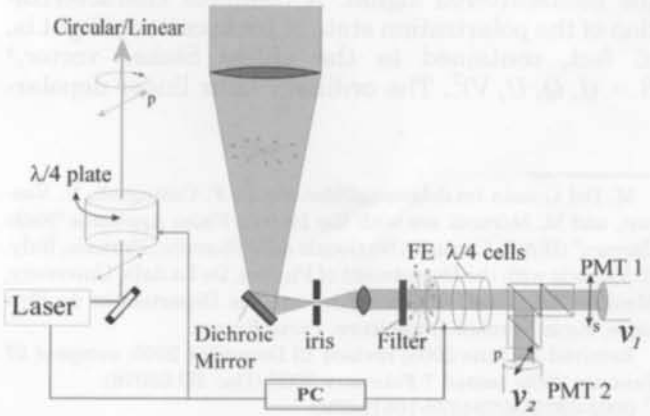


Fig. 1. Polarimetric lidar.

for each logic state:

$$\mathbf{M}_{\mathrm{FE}}{}^{\mathrm{ON}}=\begin{bmatrix}1&0&0&0\\0&0&0&-1\\0&0&1&0\\0&1&0&0\end{bmatrix},\qquad \mathbf{M}_{\mathrm{FE}}{}^{\mathrm{OFF}}=\begin{bmatrix}1&0&0&0\\0&1&0&0\\0&0&0&1\\0&0&-1&0\end{bmatrix}. \tag{4}$$

By applying a 3 bit transistor–transistor logic code to the stack of three FE cells, we could obtain different relative overall phase shifts between the two components to be analyzed ($p$ and $s$). Three special combinations of the FE cells were used for the polarimetric lidar:

$$\mathbf{M}_{\mathrm{FE}}=\underset{\text{OFF–OFF–ON}}{\begin{bmatrix}1&0&0&0\\0&0&0&1\\0&0&-1&0\\0&1&0&0\end{bmatrix}},\qquad \mathbf{M}_{\mathrm{FE}}=\underset{\text{OFF–OFF–OFF}}{\begin{bmatrix}1&0&0&0\\0&1&0&0\\0&0&0&-1\\0&0&1&0\end{bmatrix}},$$

$$\mathbf{M}_{\mathrm{FE}}=\underset{\text{ON–OFF–ON}}{\begin{bmatrix}1&0&0&0\\0&0&1&0\\0&1&0&0\\0&0&0&-1\end{bmatrix}}. \tag{5}$$

The logic states of the cells are indicated below the three matrices: In general, in this work the first cell illuminated by the light beam is written first.

With the three FE cell combinations [Eqs. (5)], the ratios of the PMT voltage signals, $v_1$ and $v_2$, are combinations of the elements of Stokes vector $\mathbf{S}$ of the backscattered light:

$$\text{Cells OFF–OFF–OFF:}\quad G\frac{v_1}{v_2}=\frac{I-Q}{I+Q} \tag{6}$$

(this ratio is the usual lidar linear depolarization $\delta_l$ when a linearly polarized laser is used),

$$\text{Cells ON–OFF–ON:}\quad G\frac{v_1}{v_2}=\frac{I-U}{I+U}, \tag{7}$$

$$\text{Cells OFF–OFF–ON:}\quad G\frac{v_1}{v_2}=\frac{I-V}{I+V}, \tag{8}$$

where $G$ is the ratio between the two PMT sensitivities, $G = G_2/G_1$. This ratio was carefully measured, as described in Appendix A.

If we assume a unitary Mueller matrix $\mathbf{M}_{\mathrm{DM}}$ for the ideal dichroic mirror, the normalized components $Q/I$, $U/I$, and $V/I$ of the backscattered light, $\mathbf{S}$, can immediately be retrieved from the three $v_1/v_2$ signal ratios [Eqs. (6)–(8)]:

$$\frac{\mathbf{S}}{I}=\begin{bmatrix}1\\\mathbf{Q}/I\\\mathbf{U}/I\\\mathbf{V}/I\end{bmatrix}=\begin{bmatrix}1\\(1-Gv_1/v_2)(1+Gv_1/v_2)_{(\mathrm{OFF\text{–}OFF\text{–}OFF})}\\(1-Gv_1/v_2)(1+Gv_1/v_2)_{(\mathrm{ON\text{–}OFF\text{–}ON})}\\(1-Gv_1/v_2)(1+Gv_1/v_2)_{(\mathrm{OFF\text{–}OFF\text{–}ON})}\end{bmatrix}. \tag{9}$$

In the actual case of nonideal optical parts, normalized Stokes vector $\mathbf{S}/I$ can still be derived if Mueller matrices $\mathbf{M}_{\mathrm{DM}}$ and $\mathbf{M}_{\mathrm{FE}}$ are known experimentally. To characterize these matrices, we transformed the lidar into a simple polarimeter and analyzed the Mueller matrices of the single optical parts (see Appendix A). Once Mueller matrices $\mathbf{M}_{\mathrm{DM}}$ and $\mathbf{M}_{\mathrm{FE}}$ were obtained, the normalized Stokes vector, $\mathbf{S}/I$, of the backscattered light could be derived as a linear combination of all three $v_1/v_2$ signal ratios [Eqs. (6)–(8)] rather than from only one of these measurements, as stated in the simplified Eq. (9). For this reason, even when only a subset of elements of $\mathbf{S}/I$ is required (as in the rest of this work), all three $v_1/v_2$ signal ratios [Eqs. (6)–(8)] and thus all the elements of $\mathbf{S}/I$ are measured.

By interweaving the three cell configurations [Eqs. (5)] during a lidar measurement, we derived this way in which the average Stokes vector $\mathbf{S}$ of the light is received by the telescope. This process was fully automated in the instrument described. Also, a continuous check of $v_1$ and $v_2$ was automatically performed on line, and the laser power was adjusted accordingly to prevent saturation of the two PMTs under all conditions.

### 3. Circular versus Linear Depolarization in Clouds

In the lidar described, the emitted Stokes vector could be either $\mathbf{S}_0 = [1\ \ 1\ \ 0\ \ 0]^T$ (linear polarization) or $\mathbf{S}_0 = [1\ \ 0\ \ 0\ \ 1]^T$ (right-hand-circular polarization). The two polarization states were obtained by means of a PC-driven $\lambda/4$ plate installed at the laser exit on a bistable mounting. With a fixed $\mathbf{S}_0$, we used the three FE combinations [Eqs. (5)] sequentially to obtain $\mathbf{S}$. We then repeated the same sequence cyclically for the other laser polarization state $\mathbf{S}_0$ to measure both linear and circular depolarization from the atmosphere.

When linearly polarized laser light is sent into the atmosphere, the ordinary linear depolarization ratio is given by Eq. (1). When the laser beam is right-hand-circularly polarized, a circular depolarization can be defined as the ratio between the right-hand- ($v_2$) and the left-hand- ($v_1$) circularly polarized signals obtained by means of a circular-polarization analyzer:

$$\delta_c=\frac{v_2}{Gv_1}=\frac{I+V}{I-V}. \tag{10}$$

In the (common) case in which the scattering media show a rotational symmetry about the lidar axis, and particles and mirror particles with respect to any plane through the axis or perpendicular to the axis exist in equal number, the Mueller matrix for 180° backscatter has the following simple form[8,9]:

$$\mathbf{M}_{\mathrm{ATM}} = \begin{bmatrix} a_1 & 0 & 0 & 0 \\ 0 & a_2 & 0 & 0 \\ 0 & 0 & -a_2 & 0 \\ 0 & 0 & 0 & a_1 - 2a_2 \end{bmatrix}. \tag{11}$$

This is true when the cloud is composed of particles with a plane of symmetry and is randomly oriented, as occurs in most cirrus and liquid clouds. Another instance of this rule is a cloud of horizontally oriented ice plates probed with a zenith-pointing lidar. A simple relationship between $\delta_c$ and $\delta_l$ exists in all these cases[9]:

$$\delta_c = \frac{2\delta_l}{1 - \delta_l}. \tag{12}$$

This relation comes from basic rules of symmetry and does not depend on the shape and optical properties of particles.

When the lidar is significantly tilted off zenith in the presence of horizontally oriented ice plates, the scattering medium becomes anisotropic along the laser beam and Eq. (12) is not strictly valid. In this way, in principle it is possible to detect the presence of those particular particles by using a nonscanning, off-zenith polarimetric lidar. For a practical application of the method, it is important to know how sensitive the method is when one is detecting oriented particles: Noise can significantly spread the ($\delta_l$, $\delta_c$) experimental points and cover any small discrepancies from Eq. (12). To be sound, the method must provide large discrepancies from Eq. (12) in the presence of oriented plates. To optimize the method, we performed a numerical scattering simulation on ice plates in search of the best choice for two instrumental parameters: the off-zenith angle of the lidar beam and the orientation of the emitted linear polarization with respect to the lidar axis.

#### 4. Numerical Simulations of Scattering by Ice Plates

Numerical scattering simulations were performed by the face-tracing technique,[10] which is derived from conventional ray tracing. In this technique, finite light beams of a known section replace the infinitesimal rays, making it possible to include Fraunhofer diffraction in the simulation and to avoid the Dirac δ peaks in the forward and backward directions. By means of this technique, the entire Mueller matrix of ice crystals was first simulated at 532 nm for ideal ice crystals illuminated by a slanted laser beam, as in Fig. 2(a). To simulate the ice plates, we used an aspect ratio (AR = $l/2a$, where $l$ is the crystal's length and $a$ is a side of the crystal) ranging from 0.2 (thin plates) to 1 (thick plates). This range covers most of the expected natural aspect ratios for plates.[11,12] Knowledge of the spatial orientations of the crystal and of the inclinations of a laser beam leading to 180° backscatter and depolarization is important for defining the optimal off-zenith angle to be used in the detection of horizontally oriented crystals. The Ψ-like plot of Fig. 2(b) shows the rotation angles, $v$, of an ideal horizontally oriented hexagonal ice plate (AR = 0.35) about its axis and the off-zenith (Φ) lidar angle leading to backscatter. $v$ is the rotation angle of the vertex of the hexagonal plate from the plane containing the laser beam and the vertical axis. The range of $v$ rotations was limited to 60° for reasons of symmetry. The $\beta_p$ and $\beta_s$ values shown are the differential backscatter cross sections of a single particle of variable ($v$, Φ) orientation that is illuminated with vertical linear polarization.

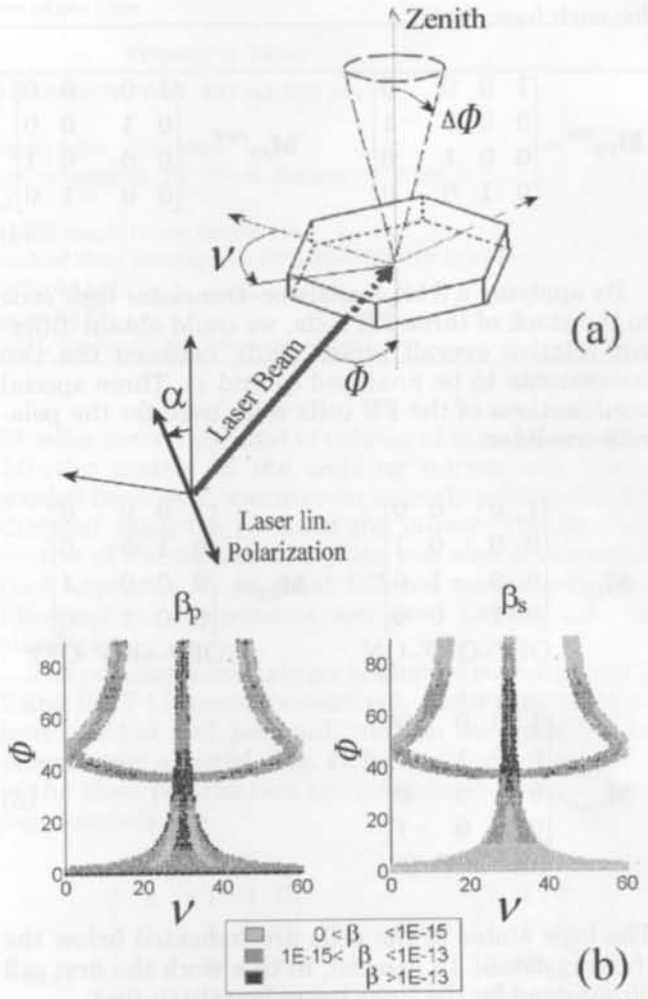


Fig. 2. (a) Scattering geometry used. (b) Rotation of a horizontally oriented plate ($l$ = 60, $a$ = 80, AR = 0.37) about its axis ($v$) and the off-zenith lidar angle (Φ) leading to parallel ($\beta_p$) and perpendicular ($\beta_s$) backscatter when the plate is illuminated with vertical linear polarization. Units are square meters per steradian for β and degrees for the angles.

In Fig. 2(b) a special ($v$, Φ) region near $v$ = 30°, Φ = 30°–40°, is characterized by a strong, highly

depolarized backscatter that is due to the corner-reflector behavior that is characteristic of ideal hexagonal crystals.[10,13] This effect involves several consecutive internal reflections of light rays on both lateral and basal faces (leading to strong depolarization) and is particularly strong in thick plates.[10] In the presence of ideal, oriented hexagonal crystals, an off-zenith lidar angle of 30°–40° is therefore expected to give a strong backscatter and depolarization, potentially providing a high signal-to-noise ratio for oriented plates. This is an alternative way to detect oriented pristine plates: one usually detects them by relying on their strong specular reflection when they are probed with zenith-pointing lidars, an effect that vanishes when one is operating just a few degrees off zenith[3] [as shown by the darkest area at $\Phi = 0$ in Fig. 2(b), left]. The detection of oriented plates by this method is highly sensitive to the presence of small quantities of oriented plates,[14]and for this reason it could overestimate the real quantitative importance of oriented plates in clouds for radiative simulations.[15]

We performed simulations for both ideal and deformed hexagonal plates, by assuming a $\Phi = 30°$ off-zenith configuration of the lidar as a logical choice for the experimental work. Because of diffraction effects, the Mueller matrix obtained by the face tracing technique is size dependent, and thus particle size was assumed to vary from 100 to 1000 μm in simulations, assuming that $0.2 < AR < 1$. Plates of these dimensions are expected to show a horizontal orientation.[15] In the model, plates were considered to be horizontally oriented, with a random rotation on their axis ($v \in [0, 360°]$) and with a random flutter of their axis of $\Delta\Phi = \pm 4°$ from the zenith. The assumed flutter is larger than that observed in most clouds by the Polarization and Directionality of the Earth's Reflectances[15,16] (POLDER) instrument ($\Delta\Phi = 0.5° 2°$) and was chosen as an upper limit for simulations. The linear laser polarization direction (parameterized with α, the angle between the polarization and the plane defined by the laser beam and the zenith) varied from $\alpha = 0°$ (vertical polarization) to $\alpha = 90°$ (horizontal polarization). Because the scattering medium is anisotropic under these scattering conditions, the linear lidar depolarization depends in fact on the laser polarization direction, α.

### A. Results for Ideal Hexagonal Ice Plates

Figure 3(a) shows the dependency of linear depolarization on α for an ideal plate with an AR of 0.25 (results for the other AR values are similar). The lidar depolarization was found to be maximum when a vertically polarized beam ($\alpha = 0$) was used and to be minimum near $\alpha = 45°$ (the linear depolarization for a randomly oriented plate that lay between the former extreme values is also shown in Fig. 3(a)]. When vertical laser polarization is used, this anisotropic effect results in a strong horizontal displacement of ($\delta_l$, $\delta_c$) points to the right of the Eq. (12) line, as shown in Fig. 3(b). By making a correct choice of the laser linear polarization direction, it is possible to take advantage of the expected displacement of the

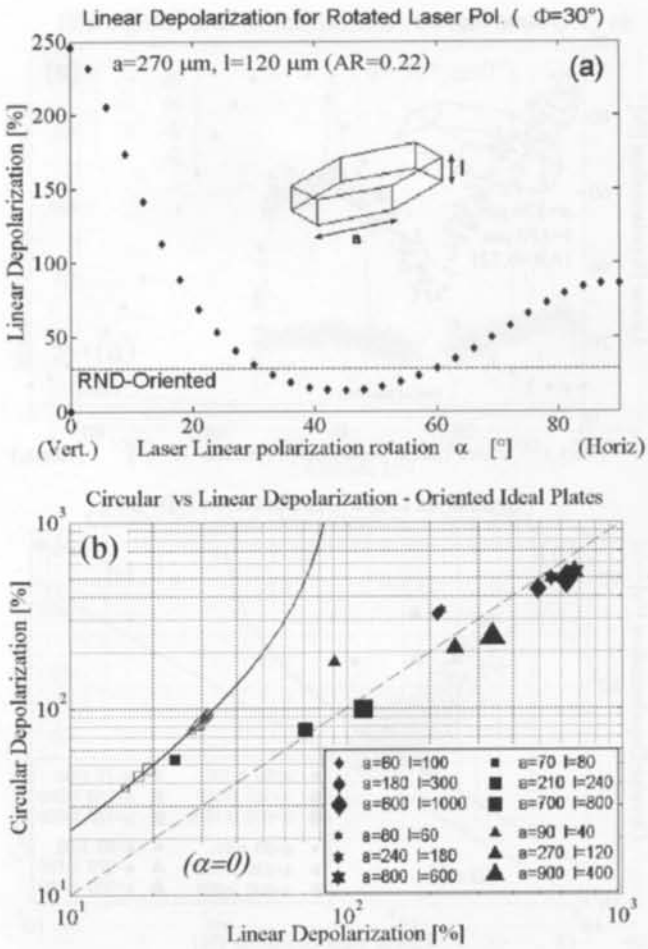


Fig. 3. Simulations for ideal hexagonal oriented plates: (a) $\delta_l$ as a function of laser linear polarization direction α (AR = 0.22); $\delta_l$ for random (RND) orientation is also shown. (b) Simulated ($\delta_l$, $\delta_c$) points for $\alpha = 0$ as obtained for several ARs and sizes. Open symbols show results for the same particles but in random orientation.

($\delta_l$, $\delta_c$) points from Eq. (2) for detecting horizontally oriented crystals of ideal geometry. Figure 3(b) shows that linear depolarizations much higher than 100% (otherwise unrealistic in zenith-pointing lidars) could be obtained in the presence of ideal oriented plates of many different ARs and sizes. This result agrees with previous numerical[17] and lidar[18] findings for a 30° off-zenith lidar.

Another result of these simulations is that the backscatter per particle in oriented plates probed with a 30° off-zenith lidar is expected to be one to four times greater than the backscatter of the same particle when the same particle is randomly oriented. This result, which is due to the corner-reflector effect, is valid for all the ARs and sizes simulated in the present work. This result means that the unusual depolarization signature of oriented ideal plates [Fig. 2(b)] could be detected in the realistic case in which oriented plates are accompanied by a similar concentration of randomly oriented crystals. When oriented plates are only a small fraction ($10^{-3}$–$10^{-2}$) of the total, detection would become difficult, if not impossible.

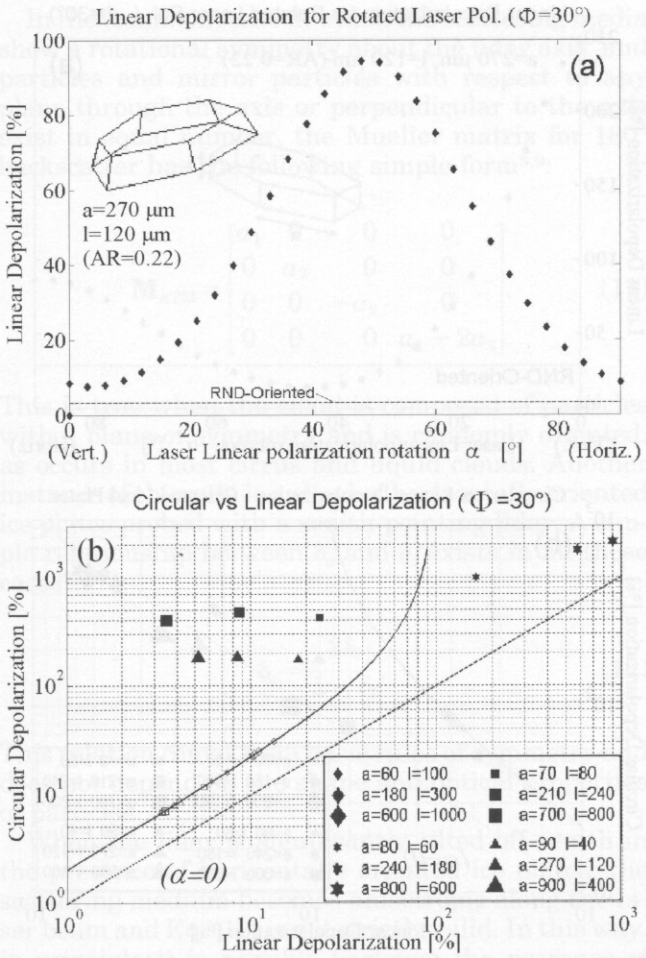


Fig. 4. Deformed, oriented hexagonal plates: (a) linear depolarization $\delta_l$ as a function of the laser linear polarization direction $\alpha$ (AR = 0.22). $\delta_l$ for random (RND) orientation is also shown. (b) Simulated ($\delta_l$, $\delta_c$) points for $\alpha = 0$ for several ARs and sizes. Open symbols show results for the same particles but in random orientation.

### B. Results for Deformed Oriented Plates

We simulated deformed plates by randomly deforming the spatial positions of the vertices of the ideal plates described in Subsection 4.A. After the deformation, we then rearranged the coordinates of some vertices to retain the polyhedral shape of the particle (plane faces), as shown in Fig. 4(a). The random deformation used was within 1/20 of the particle diameter, which was chosen arbitrarily to test the effect of moderate deformation. The Mueller matrices for five random deformations of the same particle were averaged to produce an average Mueller matrix for each AR and size.

Results in terms of ($\delta_l$, $\delta_c$) for vertical laser polarization for plates with $0.2 < AR < 1$ are shown in Fig. 4. Simulations showed a change in the behavior of lidar depolarization with $\alpha$, compared with what is shown in Fig. 3(a). Deformed plates showed a marked depolarization peak near $\alpha = 45°$. ($\delta_l$, $\delta_c$) points for vertical laser linear polarization [Fig. 4(b)] showed no clear trends in a displacement of the points about Eq. (12). Points are scattered on both sides of Eq. (12), depending on their AR. For a fixed AR, the displacement from Eq. (12) increases with particle size. These simulations showed that even small deformations of the plates could lead to relevant effects on their polarimetric behavior.

## 5. Lidar Experiments

Experimental tests were initially carried out with a zenith-pointing polarimetric lidar ($\Phi = 0°$). In a second phase, we adopted a $\Phi = 30°$ off-zenith operation, using a vertical linear polarization ($\alpha = 0°$). To do this, we tilted the whole lidar structure, avoiding the use of a scanning mirror, which would have complicated the Mueller matrix of the instrument.

We collected lidar profiles obtained with the three FE cell settings and the two laser polarizations automatically to derive the vertical profiles of **S** and its derived quantities, $\delta_l$ and $\delta_c$. For each FE cell configuration, eight lidar shots were averaged before we passed on to the next cell configuration. The process was repeated cyclically until the expected number of lidar shots was reached. This means that the **S** components $I$, $Q$, $U$, and $V$ were not measured simultaneously but were interwoven with a time delay of 1 s because of the mechanical switching time of the emitter plate. Each lidar profile was the result of averaging 48 shots for each FE cell emitter's $\lambda/4$ plate configuration. All lidar profiles were obtained with a range resolution of 7.5 m, and the ($\delta_l$, $\delta_c$) points shown in the scatter plots of Figs. 5–8 all refer to single 7.5 m lidar samples.

### A. Case Study 1: Mixed-Phase Altocumulus Cloud, $\Phi = 0°$, $\alpha = 0°$

On 17 February 2003, an ice-precipitating altocumulus cloud was observed for a duration of nearly 6 h. Figure 5(a) shows a typical profile obtained with OFF–OFF–OFF cells (equivalent to ordinary polarization lidar data) together with $\delta_l$ and $\delta_c$ profiles for a sample cloud measurement.

From the $\delta_l$ plot it is evident that the top of the cloud was a liquid, optically dense layer in which depolarization increased owing to multiple scattering. The lowest part of the cloud was an ice virga showing a $\delta_l$ typical of cirrus clouds (25%–30%). In the precipitation, particles were probably randomly oriented because no optical effects characteristic of oriented crystals were observed during the entire measurement. In fact, Fig. 5(b), which collects all the ($\delta_l$, $\delta_c$) points measured during the experiment (each point corresponds to a sample of 7.5 m), shows good agreement throughout the cloud between the experimental points and Eq. (12).

### B. Case Study 2: Cirrus Cloud, $\Phi = 30°$, $\alpha = 0°$

On 4 November 2004, a cirrus cloud was observed for a duration of 7 h. The $\delta_l$ plot shows a relatively constant depolarization, ranging from 15% to 30%. Figure 6(b) shows good agreement between the ($\delta_l$, $\delta_c$) experimental scatter plot and Eq. (12) throughout the cloud data set. This result indicated that no signi-

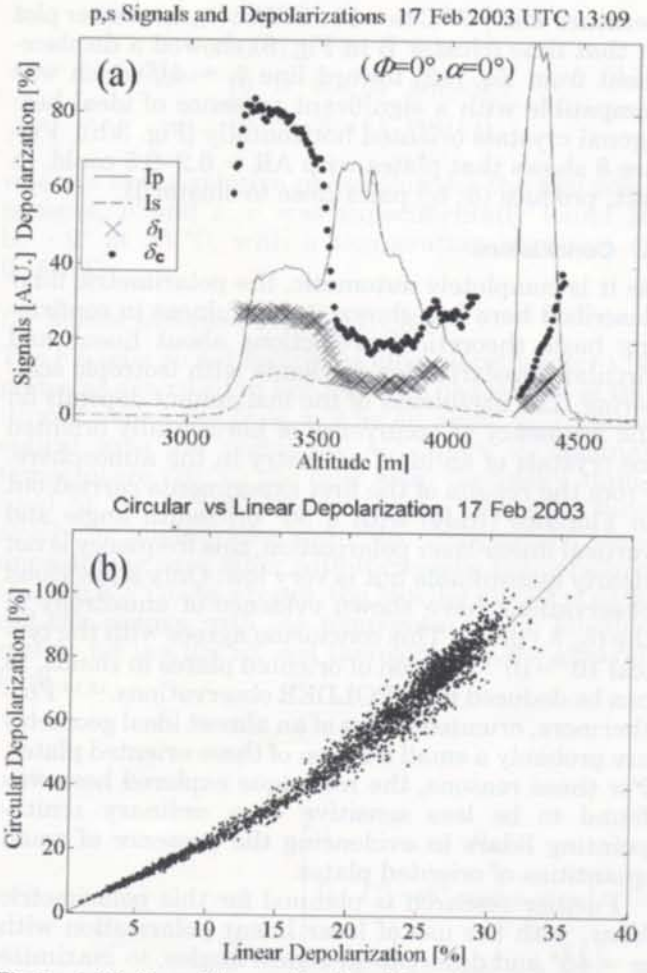


Fig. 5. (a) Ordinary lidar profiles $I_p$ and $I_s$ as obtained with linear laser polarization, and ($\delta_l$, $\delta_c$) for a sample cloud measurement. (b) Scatter plot of ($\delta_l$, $\delta_c$) for the entire 17 February 2003 cloud event.

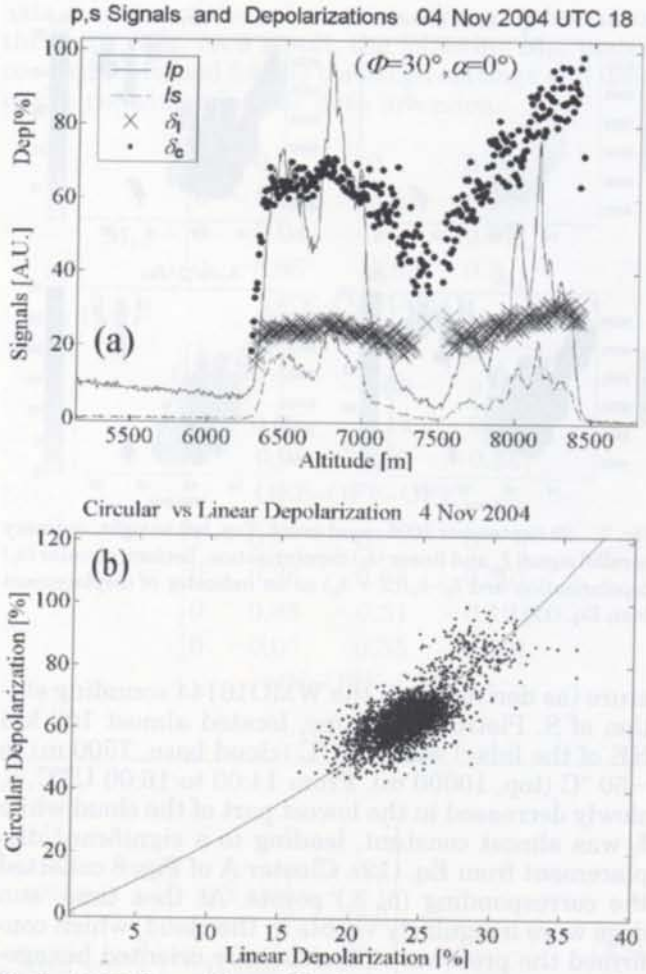


Fig. 6. (a) Ordinary lidar profiles $I_p$ and $I_s$ as obtained with linear laser polarization, and $\delta_l$ and $\delta_c$ depolarizations (Dep) for a sample measurement. (b) Scatter plot of ($\delta_l$, $\delta_c$) for the whole 4 November 2004 cloud event.

ficant amounts of horizontally oriented ideal ice crystals were present. In fact, no optical effects characteristic of oriented crystals were observed during the measurement. In this case study and for most other cirrus clouds investigated by the polarimetric lidar, $\delta_l$ was found to be in the 20%–30% range, i.e., smaller than the average $\delta_l$ obtained in the extended Facility for Atmospheric Remote Sensing data set.[14] This difference could be attributed to either use of different methods of calibration or the geographic variability of $\delta_l$.[14] Of a total of 150 h of cirrus and altocumulus measurements carried out with a 30° off-zenith configuration from August 2004 to May 2005, ~95% of the measurements showed good agreement between the ($\delta_l$, $\delta_c$) experimental points and the line of Eq. (12), indicating a local rarity of horizontally oriented ideal ice plates. This result is apparently in contrast with the POLDER observation that more than 50% of high clouds show evidence of the presence of oriented plates.[16] This apparent contrast disappears if we consider that the typical effective fraction of oriented plates in clouds as observed by the POLDER instrument is $10^{-3}$ to $10^{-2}$.[15] Hexagonal plates of ideal shape are probably a small fraction of these plates. When operating 30° off zenith, oriented plates of ideal geometry produce a backscattered intensity that is comparable with that of randomly oriented plates. Thus their presence could be observed on the ($\delta_l$, $\delta_c$) plot only when their relative concentration in the cloud is significant. Therefore the polarimetric lidar often failed in the detection of oriented plates simply because the actual concentration of ideal plates was very low.

### C. Case Study 3: Cirrus and Altocumulus, $\Phi = 30°$, $\alpha = 0°$

On 29 September 2004, cirrus fibratus clouds and altocumulus clouds were observed for a total of ~7 h. Figure 7 shows the time–height evolution of the clouds in terms of parallel intensity ($I_p$) and depolarization. The quantity $\delta_l - \delta_c/(2 + \delta_c)$ is also shown as an indicator of displacement for the measured ($\delta_l$, $\delta_c$) points from Eq. (2). This quantity is null in the ($\delta_l$, $\delta_c$) points that fall along Eq. (12).

Before 13:30 UTC, the ($\delta_l$, $\delta_c$) points agreed with Eq. (12), thus indicating the dominating presence of isotropic scatterers. At that time, the cloud temper-

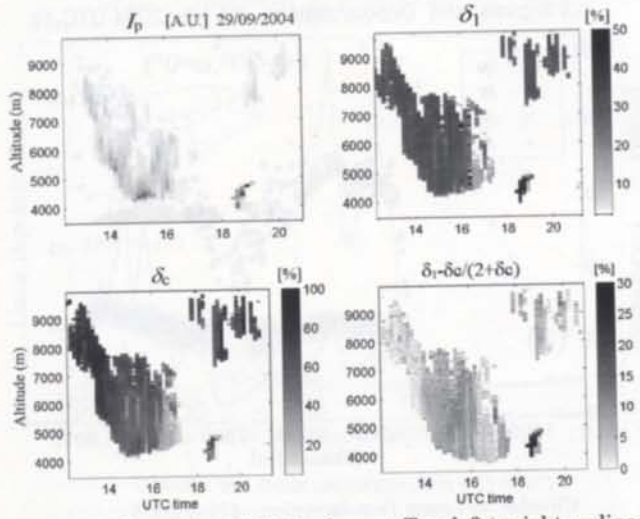


Fig. 7. 29 September 2005 cloud event. Top, left to right, ordinary parallel signal $I_p$ and linear ($\delta_l$) depolarization; bottom, circular ($\delta_c$) depolarization and $\delta_l - \delta_c/(2 + \delta_c)$ as an indicator of displacement from Eq. (12).

ature (as derived from the WMO16144 sounding station of S. Pietro Capofiume, located almost 100 km NE of the lidar) was −29 °C (cloud base, 7500 m) to −50 °C (top, 10000 m). From 14:00 to 16:00 UTC, $\delta_c$ slowly decreased in the lowest part of the cloud while $\delta_l$ was almost constant, leading to a significant displacement from Eq. (12). Cluster A of Fig. 8 collected the corresponding ($\delta_l$, $\delta_c$) points. At that time, sun dogs were irregularly visible in the cloud, which confirmed the presence of horizontally oriented hexagonal ice plates. The cloud temperature was −7 °C (base, 4500 m) to −30 °C (top, 8000 m). As cluster A showed only a slight discrepancy with theory [Eq. (12)], the actual concentration of ideal hexagonal ice crystals in the cloud was necessarily small.

A second, different phenomenon occurred on the same day from 18:00 to 19:00, when an altocumulus cloud showed a larger than usual $\delta_l$. The cloud temperature was −7 °C to −10 °C. The ($\delta_l$, $\delta_c$) scatter plot at that time (cluster B in Fig. 8) showed a displacement from Eq. (12) toward line $\delta_l \approx \delta_c$, which was compatible with a significant presence of ideal hexagonal crystals oriented horizontally [Fig. 3(b)]. Figure 8 shows that plates with AR ≈ 0.2–0.5 could, in fact, produce ($\delta_l$, $\delta_c$) pairs close to cluster B.

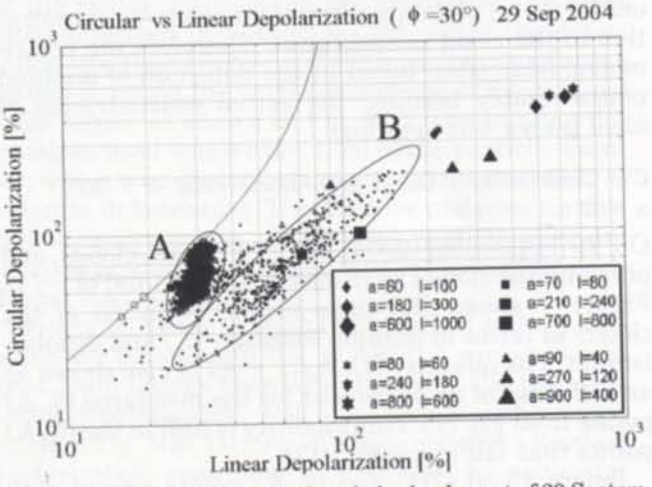


Fig. 8. ($\delta_l$, $\delta_c$) scatter plot for the whole cloud event of 29 September 2004. The simulated points for ideal plates [Fig. 3(b)] are shown for comparison.

## 6. Conclusions

As it is completely automatic, the polarimetric lidar described here has shown its usefulness in confirming basic theoretical predictions about linear and circular depolarization in clouds with isotropic scattering. The usefulness of the instrument depends on the frequency of occurrence of horizontally oriented ice crystals of an ideal geometry in the atmosphere. From the results of the first experiments carried out in Florence (Italy) with a 30° off-zenith angle and vertical linear laser polarization, this frequency is not clearly quantifiable but is very low: Only a few cloud observations have shown evidence of anisotropy in the ($\delta_l$, $\delta_c$) plane. This conclusion agrees with the typical $10^{-3}$–$10^{-2}$ fraction of oriented plates in clouds, as can be deduced from POLDER observations.[15,16] Furthermore, oriented plates of an almost ideal geometry are probably a small fraction of these oriented plates. For these reasons, the technique explored here was found to be less sensitive than ordinary zenith-pointing lidars in evidencing the presence of small quantities of oriented plates.

Further research is planned for this polarimetric lidar, with the use of laser linear polarization with $\alpha = 45°$ and different off-zenith angles, to maximize the sensitivity of this technique for the detection of oriented but irregular plates.

## Appendix A. Testing the Polarimetric-Lidar Optical Elements

### A. Testing Optical Elements of the Receiver with LED Light

To characterize the optical elements of the system, we used a parallel beam of green light. It was produced by a 525 nm, high-intensity LED with periodic rectangular pulses of 10–50 μs duration. The LED was installed in the focus of an assembly that included a lens, a linear polarizer, and a λ/4 plate to produce a parallel light beam of a known polarization state. When the telescope with a beam of known polarization state was illuminated, the lidar polarization assembly, which consisted of a mechanical ensemble of cube polarizers and two PMTs, was rotated on its axis from 0° to 90° to allow us to measure the $v_1$ and $v_2$ signals at different rotation angles by use of a digital oscilloscope. In this way, we measured the Mueller matrix of each optical element with sufficient accuracy for lidar studies simply by removing the other optical elements.

### B. Dichroic Mirror Mueller Matrix

The Mueller matrix ($\mathbf{M}_{DM}$) of the dichroic mirror was assumed to be of the form

$$\mathbf{M}_{\mathrm{DM}} = \begin{bmatrix} 1 & 0 & 0 & 0 \\ 0 & 1 & 0 & 0 \\ 0 & 0 & \cos(\upsilon) & \sin(\upsilon) \\ 0 & 0 & \sin(\upsilon) & \cos(\upsilon) \end{bmatrix}, \tag{A1}$$

where $\upsilon$ is the relative phase shift for the two components, $p$ and $s$. $\upsilon$ was experimentally found to be $-9°$ at 25 °C, with a temperature variation of 0.1%/°C.

### C. Mueller Matrices Ferroelectric Cells

The FE cells do not behave as ideal, zeroth-order $\lambda/4$ plates as described in Eqs. (4): The phase shift of the $i$th cell may differ from $\pi/2$ by an angle $\gamma_i$. The two optical axes are nominally 45° apart at nominal temperature (20 °C; the cells were thermally stabilized at 20 ± 2 °C). However, the two axes turn slowly by angles $+\mathrm{d}\omega$ and $-\mathrm{d}\omega$, respectively, thus approaching each other with increasing temperature ($\mathrm{d}\omega \sim 0.4°/°\mathrm{C}$). As a result, the Mueller matrix of each cell can change with the temperature. The Mueller matrix for the $i$th FE cell therefore has the general form

$$\mathbf{M}_{\mathrm{FE}_i} = \begin{bmatrix} 1 & 0 & 0 & 0 \\ 0 & C^2 + S^2 \cos\left(\gamma_i + \frac{\pi}{2}\right) & CS\left[1 - \cos\left(\gamma_i + \frac{\pi}{2}\right)\right] & -S \sin\left(\gamma_i + \frac{\pi}{2}\right) \\ 0 & CS\left[1 - \cos\left(\gamma_i + \frac{\pi}{2}\right)\right] & S^2 + C^2 \cos\left(\gamma_i + \frac{\pi}{2}\right) & C \sin\left(\gamma_i + \frac{\pi}{2}\right) \\ 0 & S \sin\left(\gamma_i + \frac{\pi}{2}\right) & -C \sin\left(\gamma_i + \frac{\pi}{2}\right) & \cos\left(\gamma_i + \frac{\pi}{2}\right) \end{bmatrix}, \tag{A2}$$

where

$$\begin{bmatrix} C = \cos\left[2\left(\frac{\pi}{4} + \mathrm{d}\omega\right)\right] \\ S = \sin\left[2\left(\frac{\pi}{4} + \mathrm{d}\omega\right)\right] \end{bmatrix} \quad \text{ON } i\text{th cell},$$

or

$$\begin{bmatrix} C = \cos(2\mathrm{d}\omega) \\ S = \sin(2\mathrm{d}\omega) \end{bmatrix} \quad \text{OFF } i\text{th cell}.$$

Each ON–OFF combination of the three cells produces a Mueller matrix: $\mathbf{M}_{\mathrm{FE}} = \mathbf{M}_{\mathrm{FE}_3} \cdot \mathbf{M}_{\mathrm{FE}_2} \cdot \mathbf{M}_{\mathrm{FE}_1}$. $\mathbf{M}_{\mathrm{FE}}$ was measured experimentally for the various cell configurations used in this work by the LED flasher with different polarization states. In each measurement we gradually rotated the polarization assembly by 90° to measure the axis ratio and the axis direction of the polarization ellipse at the exit of the three cells. As a result, the following $\mathbf{M}_{\mathrm{FE}}$ matrices were obtained for the three cell settings and used in the polarimetric lidar data inversion:

$$\mathbf{M}_{\mathrm{FE}} = \begin{bmatrix} 1 & 0 & 0 & 0 \\ 0 & -0.303 & 0.02 & 0.95 \\ 0 & -0.04 & -1 & 0.01 \\ 0 & 0.95 & -0.03 & 0.3 \end{bmatrix},$$

OFF–OFF–ON

$$\begin{bmatrix} 1 & 0 & 0 & 0 \\ 0 & 1 & -0.08 & 0.03 \\ 0 & 0.02 & -0.14 & -0.99 \\ 0 & 0.08 & 0.99 & -0.14 \end{bmatrix},$$

OFF–OFF–OFF

$$\begin{bmatrix} 1 & 0 & 0 & 0 \\ 0 & 0.36 & 0.88 & 0.30 \\ 0 & 0.93 & -0.31 & -0.19 \\ 0 & -0.07 & 0.35 & -0.93 \end{bmatrix}.$$

ON–OFF–ON

### D. Photomultiplier Tube Gain Ratio

Calibration of lidar depolarization is not a standard process, and the different methods used could account for some of the geographical spread of lidar depolarization values observed in cirrus clouds. In ordinary lidars it is often impossible to verify the quality of the calibration. In polarimetric studies, gain ratio $G$ between the two PMTs is a critical quantity. In this experiment we measured $G$ by using unpolarized LED light pulses of 20 μs duration. The two PMT ac signals, $v_1$ and $v_2$, were measured by obtaining a gain ratio of $G_1 = v_1/v_2$. By physically exchanging the two PMTs, we measured a new gain ratio, $G_2 = v_1'/v_2'$. Regardless of the polarization state of the LED light and of small changes in the light's intensity during the measurement, the exact gain ratio $G$ was obtained as the geometric average of $G_1$ and $G_2$. Also performed to establish the trend of $G$ with the temperature. This trend was found to be $-0.5\%/°\mathrm{C}$ and was thus disregarded in our study.

### E. Emitter λ/4 Plate

The quality of the polarimetric lidar measurement relies on the quality of the polarization state of the laser beam. This, in turn, relies on the quality of both the output λ/4 plate and its mechanical mounting, as this element is used to produce, alternately, linear and circular polarizations.

A numerical simulation was performed to assess the possible effects of a misalignment of this plate on that of the measured linear and circular depolarizations, with the assumption that all the other optical elements are ideal. The results showed that, up to a ±4° error in the cell axis rotation about the theoretical position, the expected relative changes in linear and circular depolarization at the PMTs were both less than ±6% for $0.1 < \delta_l < 0.65$. For this reason, the possible effects of a misalignment of the emission retarder plate were disregarded in this work.

## References


1. K. Sassen, "Polarization in lidar," in *Lidar*, C. Weitkamp, ed. (Springer-Verlag, 2005), pp. 19–42.
2. C. M. R. Platt, "Some microphysical properties of an ice cloud from lidar observation of horizontally oriented crystals," J. Appl. Meteorol. **17,** 1220–1224 (1978).
3. L. R. Bissonette and G. Roy, "Range-height scans of lidar depolarization for characterizing properties and phase of clouds and precipitation," J. Atmos. Ocean. Technol. **18,** 1429–1446 (2001).
4. H. C. van de Hulst, *Light Scattering by Small Particles* (Wiley, 1957).
5. J. D. Houston and A. I. Carswell, "Four-component polarization measurement of lidar atmospheric scattering," Appl. Opt. **17,** 614–620 (1978).
6. B. V. Kaul, O. A. Krasnov, A. L. Kuznetzov, and I. V. Samokhvalov, "Polarization sounding of high-altitude aerosol formations," Atmos. Opt. **4,** 303–308 (1991).
7. B. V. Kaul, "Lidar determination of oriented particles in crystal clouds," Atmos. Ocean. Opt. **8,** 439–441 (1995).
8. C. V. M. Van der Mee, J. W. Hovenier, and H. C. van de Hulst, "Conditions for the elements of the scattering matrix," Astron. Astrophys. **157,** 301–310 (1986).
9. M. I. Mishchenko and J. W. Hovenier, "Depolarization of light by randomly oriented nonspherical particles," Opt. Lett. **20,** 1356–1358 (1995).
10. M. Del Guasta, "Simulation of lidar returns from ideal and deformed hexagonal ice prisms in cold cirrus by means of face tracing," J. Geophys. Res. **106,** D12, 12,589–12,602 (2001).
11. A. H. Auer and D. L. Veal, "The dimensions of ice crystals in natural clouds," J. Atmos. Sci. **26,** 919–927 (1970).
12. P. Yang, B. C. Gao, B. A. Baum, Y. X. Hu, W. J. Wiscombe, S. C. Tsay, D. M. Winker, and S. L. Nasiri, "Radiative properties of cirrus clouds in the infrared (8–13 μm) spectral region," J. Quant. Spectrosc. Radiat. Transfer **70,** 473–504 (2001).
13. A. Borovoi, I. Grishin, E. Naats, and U. Oppel, "Backscattering peak of hexagonal ice columns and plates," Opt. Lett. **25,** 1388–1390 (2000).
14. K. Sassen and S. Benson, "A midlatitude cirrus cloud climatology from the facility for atmospheric remote sensing. II. Microphysical properties derived from lidar depolarization," J. Atmos. Sci. **58,** 2103–2112 (2001).
15. F. M. Bréon and B. Dubrulle, "Horizontally oriented plates in clouds," J. Atmos. Sci. **61,** 2888–2898 (2004).
16. H. Chepfer, G. Brogniez, P. Gouloub, F. M. Bréon, and P. H. Flamant, "Observations of horizontally oriented ice crystals in cirrus clouds with POLDER-1/ADEOS-1," J. Quant. Spectrosc. Radiat. Transfer **63,** 521–543 (1999).
17. Y. Takano and K. Jayaweera, "Scattering phase matrix for hexagonal ice crystals computed from ray optics," Appl. Opt. **24,** 3254–3263 (1985).
18. V. E. Derr, N. L. Abshire, R. E. Cupp, and G. T. McNice, "Depolarization of lidar returns from virga and source cloud," J. Appl. Meteorol. **15,** 1200–1208 (1976).